Available online at www.sciencedirect.com
SCIENCE DIRECT
Acta Materialia 54 (2006) 3883–3891
Acta MATERIALIA
www.actamat-journals.com

Liquidus and solidus temperatures of Mg-rich Mg–Al–Mn–Zn alloys

M. Ohno, D. Mirkovic, R. Schmid-Fetzer *

Institute of Metallurgy, Clausthal University of Technology, Robert-Koch-Strasse, 42, D-38678 Clausthal-Zellerfeld, Germany

Received 6 September 2005; received in revised form 10 April 2006; accepted 11 April 2006
Available online 5 July 2006

Abstract

The phase equilibria and solidification process for Mg-rich Mg–Al–Mn–Zn alloys are analyzed based on a combination of computational thermochemistry and differential thermal analysis and differential scanning calorimetry measurements. Our main concern is the proper interpretation of the experimental results of thermal analysis. For a wide range of Mg-rich alloys it is demonstrated that: (i) the high-temperature signal does not represent the actual liquidus temperature and this signal is related to the phase boundary, $L + Al_8Mn_5/L + Al_8Mn_5 + (Mg)$; and (ii) the low-temperature signal in thermal analysis is associated not with the end of the solidification process but with the precipitation of γ-$Mg_{17}Al_{12}$ phase under the Scheil condition. In addition, we demonstrate that the actual solidification temperature, either at a slow cooling rate (1 K/min) or in casting, is virtually identical to the incipient melting temperature of as-cast alloys during subsequent heating.

Keywords: Magnesium alloys; CALPHAD; Phase diagram; Multicomponent solidification; Differential scanning calorimetry

1. Introduction

The Mg–Al–Mn–Zn system is the most important system as regards commercial Mg alloys comprising the AZ and AM alloy series. Phase equilibria and thermodynamic quantities in this quaternary system provide crucial information for the design and development of Mg alloys based on those series; they also form the basis for an understanding of their solidification behavior. The CALPHAD approach [1] has been recognized as a powerful method for calculating phase diagrams and thermodynamic quantities for multicomponent systems [2]. The CALPHAD method based on well-established thermodynamic parameters enables one to carry out detailed analysis of phase equilibria with a high accuracy demanded for the development and design of industrially viable alloys. The thermodynamic descriptions for Mg–Al–Mn, Mg–Al–Zn and Mg–Mn–Zn subsystems have been recently scrutinized and improvements have been elaborated by the present authors [3–5], with the aim of establishing the thermodynamic description for the Mg–Al–Mn–Zn quaternary system. In the present paper, we focus on the phase equilibria in the Mg–Al–Mn–Zn quaternary system and the solidification behavior of relevant Mg-rich alloys.

Thermal analysis is one of the major experimental techniques for determining the phase equilibria of alloys, and several investigations of phase equilibria of Mg alloys have been performed on the basis of thermal analysis. This technique is also used to indicate the liquidus and solidus points of commercial Mg alloys in extended datasheets [6]. In our recent study of the Mg–Al–Zn system [4], it was demonstrated that the solidification process of Mg alloys such as Mg–9 wt.% Al–1 wt.% Zn and Mg–6 wt.% Al–2 wt.% Zn alloys is far from an equilibrium process, even at extremely slow cooling rate of 1 K/min. Furthermore, based on the thermodynamic calculations, it was clarified that the thermal signal, which was interpreted as the end of the solidification process in earlier literature, is closely related to the start of monovariant reaction between liquid, Mg solid solution and γ-$Mg_{17}Al_{12}$ phases. In this regard, a proper interpretation of the experimental results

* Corresponding author. Tel.: +49 5323 72 2150; fax: +49 5323 72 3120.
E-mail address: schmid-fetzer@tu-clausthal.de (R. Schmid-Fetzer).

1359-6454/$30.00
doi:10.1016/j.actamat.2006.04.022

obtained from thermal analysis for the present quaternary system has to be addressed on the basis of thermodynamic calculations.

There are two main objectives of this paper: one is to demonstrate the reliability of the thermodynamic calculations for the Mg–Al–Zn–Mn system by comparing the calculated results with the experimental ones; the other is to present a proper interpretation of thermal analysis data for Mg-rich alloys in this quaternary system on the basis of the thermodynamic calculations. Firstly, we present a detailed comparison between the calculated and experimental results reported in the literature regarding liquidus and solidus temperatures for Mg-rich alloys. It is seen that the calculated results are in good agreement with the experimental data. Secondly, we report our own painstaking thermal analysis of AZ62 and AZ91 alloys by means of differential scanning calorimetry (DSC) and differential thermal analysis (DTA) measurements. Then, the results are analyzed on the basis of thermodynamic equilibrium and non-equilibrium calculations. It is demonstrated that there is a very common misinterpretation of the "liquidus" and "solidus" data in the experimental literature detailed in the next section. The highly accurate thermodynamic calculations indicate that the widely accepted "liquidus" temperature (determined by thermal analysis) is not the actual equilibrium liquidus and the commonly assumed or interpreted "solidus" temperature is associated not with the end of the solidification process but with the start of precipitation of γ-$Mg_{17}Al_{12}$ phase.

2. Experimental literature data

Experimental studies of the Mg-rich part of the Mg–Al–Mn–Zn quaternary system are briefly summarized in the following. The Mn solubility in liquid has been experimentally determined by Thorvaldsen and Aliravci [7]. The alloys were prepared at 770–800 °C by first adding Al and Zn, and then adding 4.5 wt.% $MnCl_2$. After alloying, the melt was held at the alloying temperature for 30–45 min in order to settle all reaction products. The temperature was then reduced to a temperature of interest, followed by holding for a minimum of 45 min in order to settle all precipitated phases. At the end of the holding period, the samples were cast directly from the crucible into a permanent mould. It was mentioned that the temperature reduction during the sampling was negligible. All the samples were analyzed using both emission spectrometry and inductively coupled plasma (ICP) spectrometry. Also, rapidly solidified melt-spun ribbons, which were produced after casting of the specimen for chemical analysis, were investigated using scanning electron microscopy (SEM)/energy dispersive X-ray analysis (EDX) to determine the composition of particles in the melts. The measured compositions of the particles were all within the range of Al_8Mn_5 phases. It should be pointed out that the solubility data reported in Ref. [7] has not been put into the perspective of the equilibrium liquidus as measured by thermal analysis. It is shown below that solubility measurement is the only method capable of determining the true liquidus of these alloys, which is clarified and quantitatively explained based on the present thermodynamic calculations.

The solidus isotherms for the Mg-rich corner have been presented by Busk and Marande [8]. However, the details of the experimental method were not explained. In their work [8], moreover, the "pseudo-solidus" isotherms, which represent the solidification temperature in normal sand-casting practice, were measured as follows. The tensile testing of an as-cast sample bar was performed with stepwise heating, holding for 10 min at each temperature step; the non-equilibrium solidus temperature was determined from the temperature at which a brittle fracture occurred.

Several thermal analyses for Mg alloys have been reported [9–12]. DSC/thermogravimetric analysis (TGA) measurements and dilatometric analysis for AZ91 and AM60 alloys were performed by Lindemann et al. [11]. A DSC plate transducer with non-sealed graphite crucibles, covered by lids, was applied. The authors reported problems due to the high reactivity and partial pressure of the Mg vapor. Yellowish coloring was observed on the transducer and crucible lid. The TGA signal also showed increased mass loss within the melting range due to Mg evaporation and a subsequent mass gain, possibly due to Mg oxidation. This required rapid experimentation with high scanning rates (10 K/min), a reduction of the melt retention time and excluded the possibility of thermal cycling of the sample. The chemical composition of the studied alloys was not presented and thus their results are not employed for comparison with thermodynamic calculations in the present paper, mainly because of uncertainty in the Mn composition of their samples. The liquidus and solidus temperatures for AZ91 and Mg–15 wt.% Al–0.4 wt.% Zn–0.2 wt.% Mn alloys were measured during a casting experiment [9]. The casting for these alloys was carried out at 710 °C and the temperature/time data during solidification were obtained using thermocouples inserted in the mould cavity and the riser. Since the solidification rate in their experiment was quite fast, it is considered that the solidification proceeds under non-equilibrium conditions. Cerri and Barbagallo [10] carried out DTA measurements for AZ91 alloys with a heating/cooling rate of 1 K/min. However, an alumina crucible was used, which is anticipated to react with the sample. In fact, several peaks appeared in the heating curve of their work [10], while only two strong peaks were observed in the work of Lindemann et al. [11] and our experiments, as discussed later. Hence, we focused on two strong peaks from the cooling curve of Ref. [10] and employed these data with care in the comparison with the calculations. The cooling curve for AZ91 alloy during casting was presented by Wang et al. [12]. The solidification process is considered to be far from the equilibrium conditions in their work [12].

In addition to the above-mentioned data, we employed the experimental results of thermal analysis provided by

Table 1
Chemical composition (wt.%) of the alloys investigated (balance Mg)

Alloy sample	Al	Zn	Mn	Si	Fe	Cu	Ni	Be
AZ62	**6.61**	**1.32**	**0.24**	0.013	0.0021	0.0028	0.0004	0.0005
AZ91	**8.67**	**0.63**	**0.21**	0.020	0.0062	0.0042	0.0005	0.0004

The compositions for the elements with we are concerned, i.e., Al, Zn and Mn are indicated in bold type.

Competence Centre Magnesium, Hydro Aluminium Research Centre [6]. They carried out conventional thermal analysis in a steel crucible using two thermocouples, one placed in the center and the other close to the crucible wall. The average cooling rate was calculated to be 1 K/s.

It should be pointed out here that the widely accepted "liquidus" and (non-equilibrium) "solidus" temperatures of these alloys are practically based on the thermal analysis data. For example, one can see that the "liquidus" and (non-equilibrium) "solidus" data in the database of the International Magnesium Association[1] are quite consistent with the thermal analysis data of the above-mentioned literature. In the present study, the "liquidus" and "solidus" data of the International Magnesium Association are not employed, since the original works containing these data were not available.

3. Experimental method and results

The chemical compositions of the Mg alloys investigated in the present work are shown in Table 1. The compositions of the elements of our concern, i.e., Al, Zn and Mn are indicated in bold type. Two master alloys, AZ91HP and AZ61 provided by Norsk Hydro Magnesiumgesellschaft mbH, Bottrop, were used for the preparation of the alloys. The compositions of the prepared alloys were analyzed using ICP spectrometry.

The DTA measurements were performed using a Netzsch DTA 404 S apparatus (Netzsch GmbH, Selb, Germany). In preliminary experiments, it was realized that because of the high oxygen affinity and vapor pressure of the Mg alloys studied, a special adaptation of the DTA equipment using a sealed Ta crucible was indispensable for obtaining reproducible and reliable data. The details of the adaptation can be found in Ref. [13]. For the DTA measurements, high-purity γ-Al_2O_3 powder was used as the reference material. The DTA scanning program comprised 330–670–330 °C cycles at heating/cooling rates of 1 and 5 K/min. The measurements were carried out at 5×10^{-3} mbar static chamber vacuum to protect the outer surface of the Ta capsule against oxidation and to eliminate convective heat exchange in gas inside the chamber. The overall uncertainty of the DTA measurements was estimated to be ±3 K.

The DSC measurements were performed using Setaram MHTC 96 DSC equipment (Setaram Instrumentation, Caluire, France). Helium at a 2 l/h flow rate was used as the analysis chamber gas. A sealed Ta capsule was also used for the reasons mentioned above. The reference Ta capsule contained a sapphire cylinder as reference material and was also sealed by welding. More experimental details are given in Ref. [4]. The scanning program comprised 150–700–150 °C cycles at heating/cooling rates of 3 and 5 K/min. The overall uncertainty of the DSC measurements was estimated as ±3 K.

In addition, the results of DSC measurements performed by the group of Prof. Ferro at the University of Genova were employed for comparison. These DSC measurements were obtained using a Setaram TG-DSC 111 calorimeter. The same scanning program was applied. A purified Ar flow of 2 l/min through the measuring chamber was applied. In the present paper, the experimental data of Ferro's group are referred to as DSC2, while our own DSC data (Setaram MHTC 96) are indicated as DSC1.

Table 2 shows the experimental results of the DSC and DTA measurements. Two signals, A and B, were clearly and consistently observed for both measurements. The temperature for signal A was assessed based on the onset of the signal on the cooling curve. The temperature for signal B was assessed based on the maximum of the signal on the heating curve. This point is discussed in detail in Section 5.

The microstructure of the samples after DTA experiments was examined using SEM/EDX. The samples were ground and polished down to 1 μm diamond under alcohol to avoid reaction with water. The samples were etched in a solution of 1 cm^3 HNO_3, 20 cm^3 acetic acid, 60 cm^3 ethylene glycol and 19 cm^3 H_2O for 15 s at room temperature. The results of microstructural observations are discussed in Section 5.

4. Thermodynamic description

As mentioned in Section 1, the thermodynamic description of the Mg–Al–Mn system has been improved, based mainly on the experimental data for Mn solubility in liquid [3]. The thermodynamic description of the entire Mg–Al–Zn system has been reported by Liang et al. [14] and the high reliability for the Mg-rich corner has been demonstrated by the present authors [4]. As for the Mn–Zn binary system, we used the thermodynamic parameters of Miettinen [15], and the thermodynamic calculation for the Mg–Mn–Zn ternary system was performed and reported in Ref. [5]. These thermodynamic descriptions for the subternary systems were employed in the present calculations. For the remote ternary edge system Al–Mn–Zn, the thermodynamic description has not been established and, in

[1] http://www.intlmag.org/phys07.aspx.

Table 2
Signal temperatures of the alloy samples evaluated by means of DSC and DTA measurements (°C)

	AZ62		AZ91	
	Signal A[a]	Signal B[b]	Signal A[a]	Signal B[b]
DSC 1 (this work)	608	424	598	434
DSC 2[c] (this work)	609	416	595	433
DTA (this work)	608	418	599	436

[a] Start of the (Mg) precipitation.
[b] Start of the γ-phase precipitation.
[c] DSC 2 is the experimental data measured with different equipment by Ferro's group.

the present study, a simple extrapolation from each edge system was adopted.

The software "Pandat"[2] [16] was employed for all the calculations in this work.

5. Calculated results and discussion

5.1. Equilibrium liquidus and solidus temperatures of quaternary alloys

The calculated vertical sections at constant Al and Zn compositions are shown in Fig. 1 with the experimental data of Thorvaldsen and Aliravci [7]. One can see that the calculated results are in good agreement with the experimental results [7]. The important point here is that the primary precipitate is Al_8Mn_5 phase at high Mn composition as observed in the SEM/EDX analysis [7].

Shown in Fig. 2(a) are the calculated polythermal solidus isotherms at 0.2 wt.% Mn with the alloy composition of the experimental data of Busk and Marande [8]. The calculated solidus corresponds to the phase boundary, (Mg) + AlMn/L + (Mg) + AlMn, at a given temperature where (Mg) denotes the Mg solid solution and AlMn represents an Al–Mn binary phase such as β-Mn, Al_8Mn_5 and $Al_{11}Mn_4$ phases. These Al–Mn binary phases are not distinguished to enhance readability. The phase field just below these isotherms is the two-phase field of (Mg) + AlMn. The adjacent phase fields are four different three-phase fields consisting of $\Sigma + X$ with $X = \gamma$-$Mg_{17}Al_{12}$, ϕ, τ or MgZn, where the symbol Σ denotes (Mg) + AlMn, and ϕ and τ phases correspond to ternary compounds modeled as $Mg_6(Al,Zn)_5$ and $Mg_{26}(Mg,Al)_6(Al,Mg,Zn)_{48}Al_1$, respectively [14]. Also shown in Fig. 2(a) are monovariant reaction lines between four phases, L + (Mg) + AlMn + X. The direction of decreasing temperature of these monovariant reaction lines is indicated by the arrows. The monovariant lines confine the range of Mg-rich alloys that solidify in equilibrium to (Mg) + AlMn. There is no single-phase field of the (Mg) solid solution beneath this solidus surface. The three partially shown triangles in Fig. 2(a) correspond to different nonvariant five-phase equilibria with L + Σ + X + Y, where X and Y are the neighboring phases. For example, the triangle at the Al-rich side corresponds to the phase field L + (Mg) + $Al_{11}Mn_4$ + ϕ + γ-$Mg_{17}Al_{12}$.

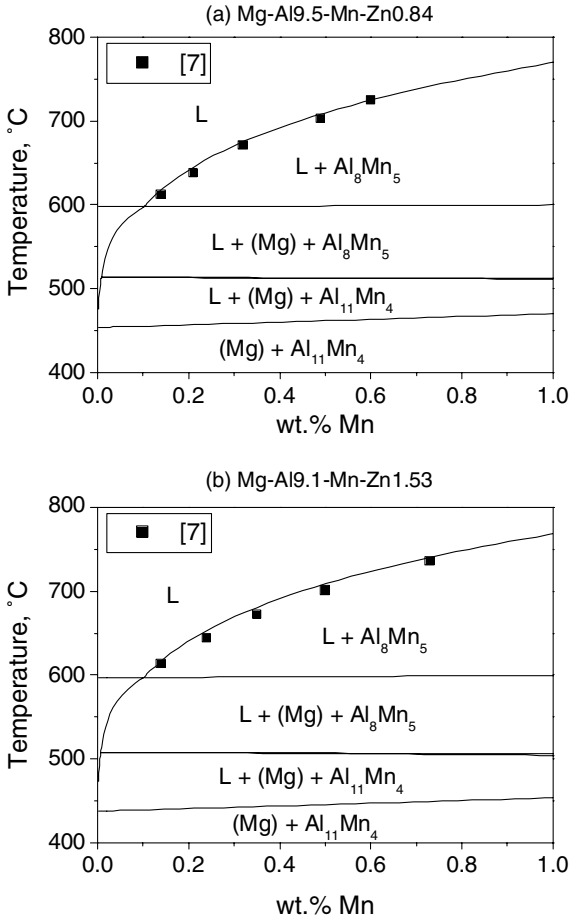

Fig. 1. Calculated vertical sections of the Mg–Al–Mn–Zn phase diagram and the experimental data of Ref. [7]. (a) Fixed 9.5 wt.% Al and 0.84 wt.% Zn. (b) Fixed 9.1 wt.% Al and 1.53 wt.% Zn.

A comparison between the calculated and experimental solidus temperatures is shown in Fig. 2(b). The vertical axis represents the experimental value, while the horizontal axis represents the calculated equilibrium value. The solid line is a visual aid, representing complete agreement. One can see that the calculated solidus temperature is fairly consistent with the experimental data. As discussed later in Section 5.2, the equilibrium solidus temperature for Mg-rich alloys cannot be simply detected in the thermal analysis and, therefore, the data of Ref. [8] must have been obtained using other techniques. It is assumed that these involved equilibration of the samples and possibly microstructural analysis, but no details are given in Ref. [8]. It is noted that Busk and Marande [8] additionally measured the non-equilibrium solidus as detailed in Section 5.3.

It is stressed that the good agreement between the calculated and the experimental results regarding liquidus and solidus temperatures supports the reliability of the present

[2] Pandat – Phase Diagram Calculation Engine for Multicomponent Systems, CompuTherm LLC, 437S. Yellowstone Dr., Suite 217, Madison, WI, USA.

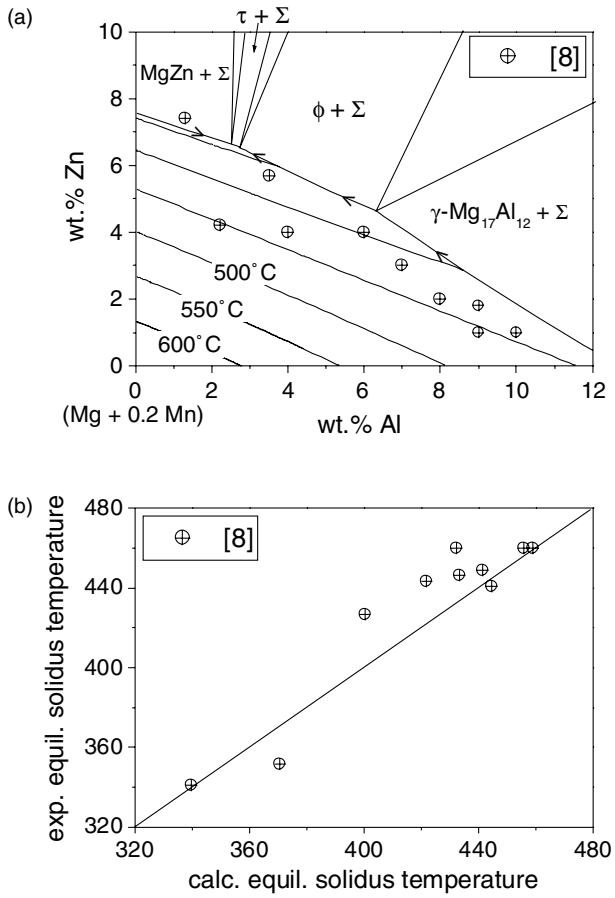

Fig. 2. (a) Mg–Al–Mn–Zn solidus isotherms calculated at constant 0.2 wt.% Mn and the sample compositions given in Ref. [8]. The solid phases in equilibrium with this last liquid are denoted by Σ (=(Mg) + AlMn); the surface of solidus isotherms terminates at the monovariant reaction lines indicated by arrows for decreasing temperature; these are four-phase equilibria, L + Σ + one additional phase. (b) Comparison between the calculated and the experimental results of solidus temperature for each sample given in (a).

thermodynamic description for the Mg-rich corner in the Mg–Al–Zn–Mn system.

5.2. Comparison with thermal analysis data

In this section, we compare the thermodynamic calculation with the experimental results of thermal analysis. As mentioned in Section 1, the main focus in this section is placed on the proper interpretation of the experimental results.

Fig. 3 demonstrates the calculated vertical sections of equilibrium phase diagrams with the experimental results of thermal analysis. Note that two signals are observed in all the thermal analyses. In this comparison, the following points should be noted. (i) The signals obtained in our experiments are virtually identical to the other experimental results, even though the cooling/heating rate in our experiment is very low (1 K/min for DTA, 3 K/min for DSC). (ii) The signal at high temperature (signal A in the present experiment) does not correspond to the liquidus temperature. This signal is closely related to the phase boundary, L + Al_8Mn_5/L + Al_8Mn_5 + (Mg). (iii) The signal at low temperature (signal B in the present experiment) disagrees with the equilibrium solidus temperatures. Points (ii) and (iii) can be well explained by the present thermodynamic calculation as discussed in the following.

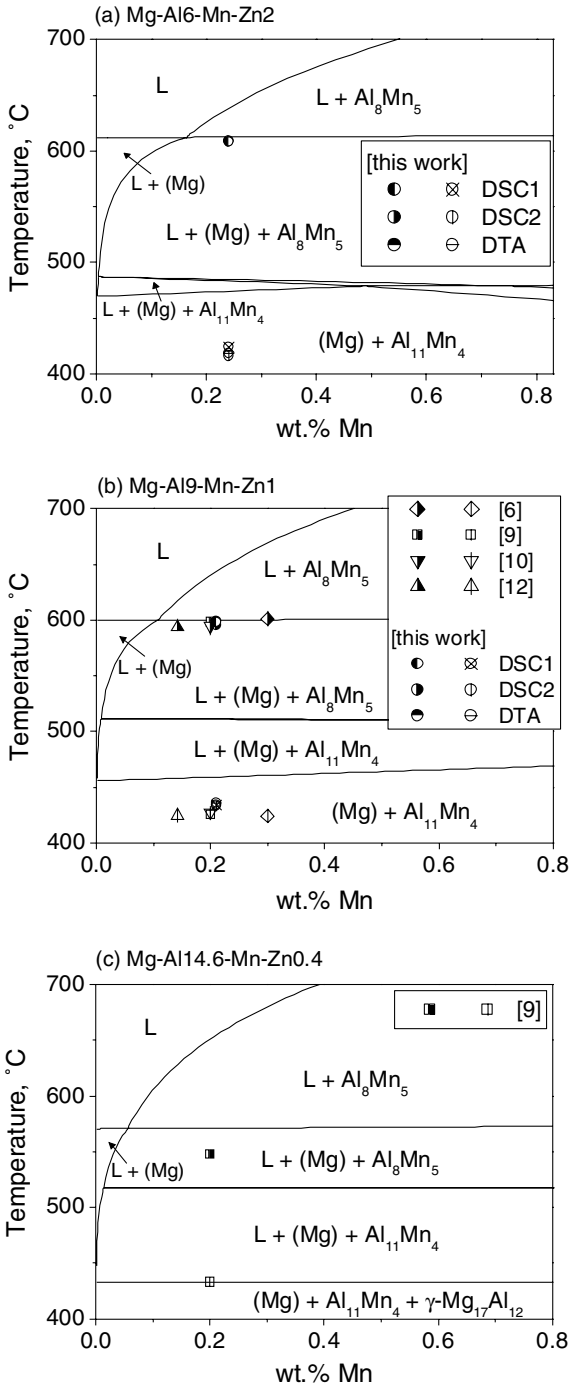

Fig. 3. Calculated vertical phase diagram sections at a given composition and the experimental results of thermal analysis: (a) Mg–6.68 wt.% Al–Mn–1.82 wt.% Zn; (b) Mg–9 wt.% Al–Mn–1 wt.% Zn; (c) Mg–14.6 wt.% Al–Mn–0.4 wt.% Zn. Half-filled and open symbols denote the highest and lowest thermal signal, respectively.

The DSC curve of our AZ91 alloy sample is shown in Fig. 4(a) and the solidification curve of this alloy calculated under equilibrium conditions is represented by the solid line in Fig. 4(b). In Fig. 4(b), the solidification starts with precipitation of Al_8Mn_5 phase at 642 °C as indicated by the arrow; however, the amount of precipitation is very small, which may not be detectable in the thermal analysis. The fraction of liquid starts to decrease markedly when Mg solid solution precipitates at 600 °C. In the thermal analysis, therefore, the precipitation of Mg solid solution was detected as signal A. In other words, although the primary precipitate at somewhat higher Mn composition is Al_8Mn_5 phase as demonstrated in Fig. 1, the high-temperature signal in the thermal analysis is related not to that equilibrium liquidus but to the phase boundary, $L + Al_8Mn_5$/$L + Al_8Mn_5 + (Mg)$. Note that in Fig. 3(c) the experimental result of Ref. [9] deviates from this phase boundary. The data of Ref. [9] represent the averaged value of the temperatures assessed from cooling curves measured at different positions in the casting equipment. The solidification at the local area of the casting equipment proceeds with different cooling rates ranging from 20 to 600 K/min and the averaged value of Ref. [9] has a large uncertainty.

Under the equilibrium condition, as shown in Fig. 4(b), the solidification ends at 475 °C which is much higher than that of signal B in Fig. 4(a). The dashed line in Fig. 4(b) represents the solidification process of the AZ91 alloy calculated under Scheil conditions. The kink of that solidification curve is observed at 431 °C and this corresponds to the precipitation of γ-$Mg_{17}Al_{12}$ phase under Scheil conditions. By comparing this behavior with the DSC curve of Fig. 4(a), it is clear that signal B is closely related to γ-$Mg_{17}Al_{12}$ precipitation. This is quite consistent with the microstructural observation as shown in Fig. 5. This represents the microstructure of the same AZ91 alloy after the DTA measurements. The dark region corresponds to the matrix of Mg solid solution. The magnification of the microstructure is shown in Fig. 6. Firstly, it should be noted that the primary precipitate Al_8Mn_5 phase is observed, in agreement with an equilibrium start of solidification. Furthermore, the coring in the Mg solid solution occurs as indicated by the different contrast of gray level, and γ-$Mg_{17}Al_{12}$ phase occurs in the microstructure.

Both coarse γ-particles, grown from the liquid, and fine γ-particles are found in the microstructure. The fine particles are grown as discontinuous precipitation from the supersaturated Mg matrix in the high-concentration region indicated by coring. Thus, the solidification and crystal growth of Mg solid solution proceeds under non-equilibrium conditions, even though the cooling rate for our measurement was extremely slow (1 K/min). This microstructural observation strongly supports the fact that signal B is related to the precipitation of γ-$Mg_{17}Al_{12}$ phase from the melt under Scheil conditions.

From a closer look at Fig. 4(a), one can see a slight temperature difference between the onset of signal B on the cooling curve and the maximum of signal B on the heating curve. This is because the supercooling effect on precipitation of γ-$Mg_{17}Al_{12}$ phase occurs during the cooling cycle. As mentioned in Section 3, the temperature for signal B has been assessed based on the maximum of the heating

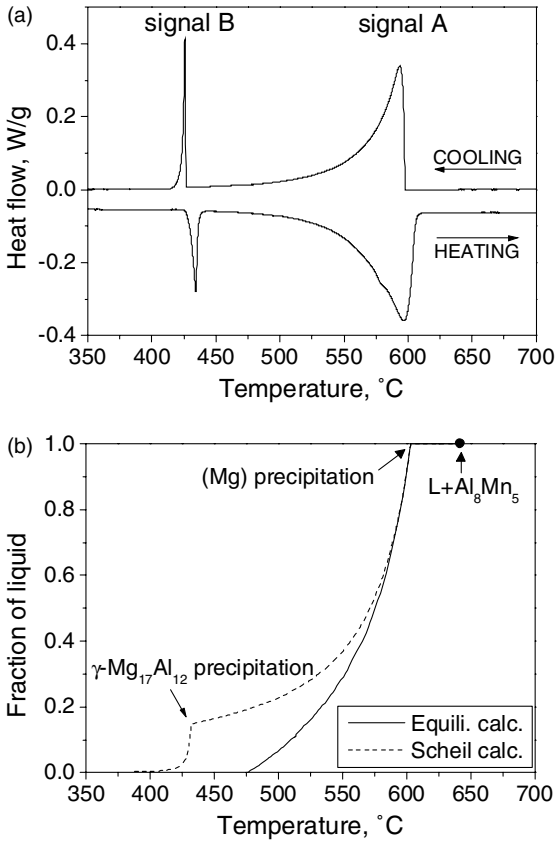

Fig. 4. (a) DSC curve of the AZ91 alloy sample (Table 1). The heating/cooling rate is 3 K/min. (b) Solidification behavior of that sample calculated by equilibrium (solid line) and Scheil (dashed line) conditions.

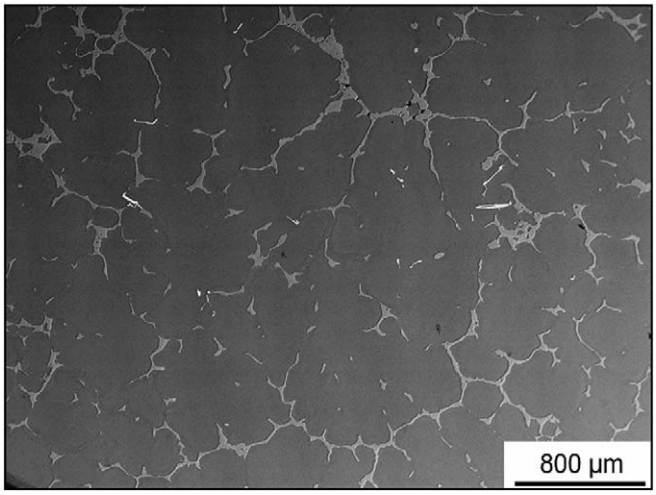

Fig. 5. Backscatter electron micrograph of the AZ91 sample solidified at 1 K/min.

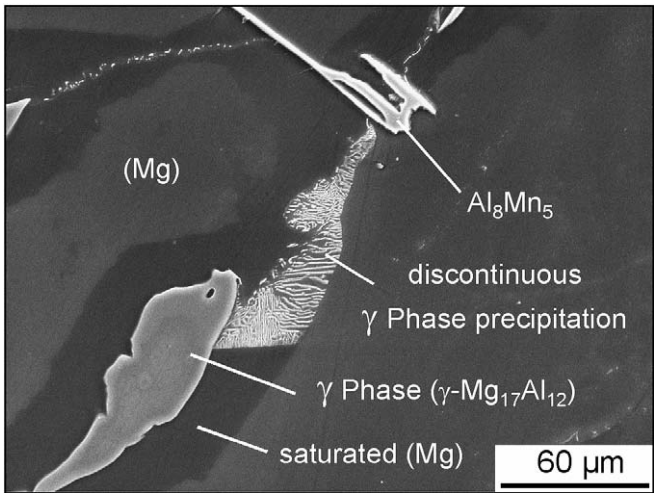

Fig. 6. Magnified section from Fig. 5. Non-equilibrium γ-phase particles are precipitated, resembling Scheil solidification conditions. Needle-alike Al_8Mn_5 particles are also observed.

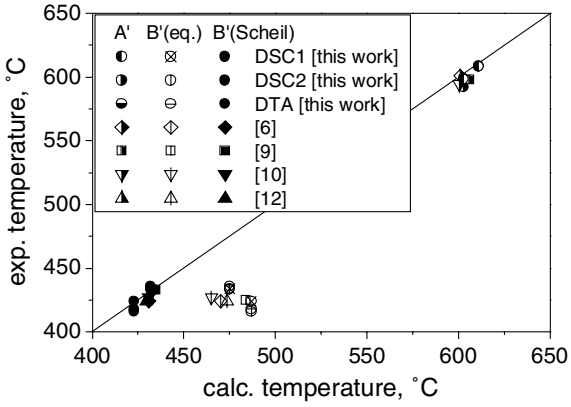

Fig. 7. Comparison between the experimental results of samples shown in Fig. 3 and different calculations. The calculated result for signal A′ represents the temperature at which the precipitation of Mg starts. The result for signal B′ (equilibrium) corresponds to the equilibrium solidus temperature. The full symbols, B′ (Scheil), denote the calculated temperature for precipitation of γ-$Mg_{17}Al_{12}$ phase under Scheil conditions. The diagonal line is a visual aid indicating perfect agreement.

curve. This temperature is related to complete melting of γ-$Mg_{17}Al_{12}$ phase during the heating cycle, which should be equivalent to the temperature at which the precipitation of γ-$Mg_{17}Al_{12}$ phase starts during the cooling cycle without supercooling effect.

Fig. 7 demonstrates the detailed comparison between the calculated results and the experimental data obtained by thermal analysis given in Fig. 3. The vertical axis represents the experimental value, while the horizontal axis represents the calculated value. The calculated result denoted as signal A′ represents the temperature for the start of (Mg) precipitation under Scheil conditions, which is virtually identical to the equilibrium phase boundary, $L + Al_8Mn_5/L + Al_8Mn_5 + (Mg)$, as shown in Fig. 4(b). The calculated values of signal A′ are compared to the experimental data for the high-temperature signal (signal A in our experimental result). The calculated value indicated as signal B′ (equilibrium) corresponds to the equilibrium solidus temperature, while the one for signal B′ (Scheil) represents the temperature for the start of γ-$Mg_{17}Al_{12}$ precipitation under Scheil conditions. These calculated results are compared to the experimental data for the low-temperature signal (signal B). One can clearly see that the calculated results for signals A′ and B′ (Scheil) are in excellent agreement with the corresponding experimental data. As mentioned in Section 2, the experimental data of Ref. [11] are not employed for the comparison shown in Figs. 3 and 7, because of the uncertainty of the Mn composition in their samples. However, provided that the Mn composition in their AZ91 alloys is in the range 0.1–0.5 wt.%, their measured high- and low-temperature signals also satisfactorily agree with the calculated signals A′ and B′ (Scheil), respectively, within an error of 3 °C. It is noted that under Scheil conditions, the solidification process terminates at much lower temperature, as discussed in the following.

5.3. Non-equilibrium solidus temperature (NEST)

The present thermodynamic calculations have demonstrated that, in practically important Mg alloys, the solidification process proceeds under Scheil conditions and, therefore, the actual solidification temperature is considered not only lower than the equilibrium solidus but even lower than signal B detected in the thermal analysis. In the work of Busk and Marrande [8], as mentioned in Section 2, the NESTs of as-cast alloys were investigated by means of tensile testing at increasing temperature. As-cast alloys consist of non-equilibrium phases originating from rapid solidification processes. Following the Scheil picture of layered crystal growth, the last layer of solid phase(s) was in local equilibrium with the last drop of the liquid phase. During heating this process may be considered reversed if solid-state diffusion is neglected. The incipient melting thus occurs at the same temperature as the non-equilibrium (Scheil) solidus, which is lower than the equilibrium solidus temperature. Such an incipient melting can be observed as a brittle fracture in tensile testing for a stepwise increased temperature. A finite amount of liquid is required, which is arbitrarily set at 2%; that is, the NEST represents the temperature at which the fraction of solid, f_s, equals 0.98 during the solidification process under Scheil conditions.

Shown in Fig. 8(a) are the solidus isotherms for NEST calculated at 0.2 wt.% Mn under Scheil conditions and the sample compositions given in Ref. [8]. The experimental data for the low-alloyed composition range are distinguished by a different symbol for the sake of convenience in the discussion. The band of isotherms up to 550 °C is presented with an interval of 10 °C. The present thermodynamic calculation shows that the NEST drastically decreases with increasing Al and/or Zn composition in the dilute composition range. In the non-dilute range, the

addition of Al has no significant effect, while the addition of Zn slightly decreases the NEST.

The actual comparison between the calculated and the experimental data is demonstrated in Fig. 8(b). The vertical axis is the experimentally determined incipient melting temperature of as-cast alloys, while the horizontal axis denotes the NEST for $f_s = 0.98$. The horizontal bar in each point represents the calculated temperature range between $f_s = 0.97$ and 0.99. Except for the data in the low-alloyed composition range specified by the half-open symbol, all the experimental data are in excellent agreement with the calculated results. Hence, it is realized that the incipient melting temperature of as-cast Mg alloys is virtually equivalent to the solidification temperature under Scheil conditions, and both the incipient melting temperature and the solidification temperature of as-cast Mg alloys are very well described and predicted by the present thermodynamic calculations.

In Fig. 8(b), the experimental data for the low-alloyed composition range take higher values than the calculated

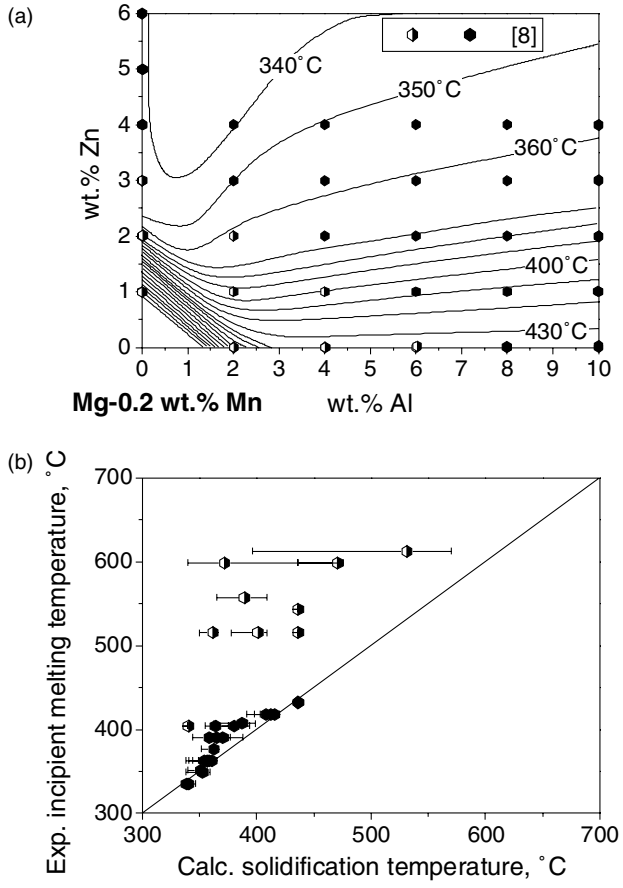

Fig. 8. (a) Isotherms for non-equilibrium solidus temperature (NEST, for fraction solid $f_s = 0.98$) calculated at 0.2 wt.% Mn under Scheil conditions and the sample compositions given in Ref. [8]. The interval of isotherms is 10 °C. For the sake of convenience, the data in the low-alloyed composition range are distinguished by half symbols. (b) Comparison between the calculated and experimental solidification temperatures. The calculated result corresponds to the temperature for $f_s = 0.98$ and the bar in each point indicates the temperature range for $f_s = 0.97$–0.99. Some ranges are so small that they are covered by the symbol size.

ones, which means that they are closer to the equilibrium values. Either the solidification of those alloys proceeds closer to equilibrium conditions or some equilibration occurs during the slow heating of the incipient melting experiments. For solidification of such low-alloyed samples under exact Scheil conditions, large composition gradients in the Mg matrix are predicted. These will be attenuated if the solid-state diffusion is not entirely blocked. Careful attention should also be paid to the fact that in the dilute composition range, the total amount of non-equilibrium solid phases, which contribute to the incipient melting during heat treatment, is quite small as compared to those in non-dilute composition range. For example, the volume fraction of non-equilibrium eutectic structure in Mg–8 wt.% Al alloy is calculated to be 0.125, while that in Mg–2 wt.% Al alloy is only 0.017, even though their calculated solidification temperature is essentially the same with a NEST value of 436 °C. Hence, even if the solidification proceeds under Scheil conditions, such a small amount of the non-equilibrium structures could be readily removed by the implied heat treatment before the incipient melting in the experimental work of Ref. [8]. In the dilute composition range, furthermore, a slight difference in the critical amount of liquid fraction, which is considered detectable in tensile testing, results in large variation of solidification temperature. The impact of varying the amount of residual liquid from 1% to 3%, thus defining the range of NEST for each alloy, is shown by the bar in each point of Fig. 8(b). It is obvious that the large bars are associated with the low-alloyed samples. These show a long and flat tail in their fraction liquid vs. temperature curve, unlike the steep drop of residual liquid in Fig. 4(b) for the AZ91 alloy.

The difference between Figs. 8(b) and 7 is emphasized. All the alloys shown in Fig. 7 belong to the high-alloyed category and their calculated NEST (398–413 °C) is thus in the range where the calculations in Fig. 8 are very well supported by experimental data. It is thus safe to assume that solidification of these alloys actually terminates at their NEST (398–413 °C). These temperatures are clearly below that of signal B′(Scheil) in Fig. 7, thus supporting the prediction that signal B does not indicate the end of the solidification process. Signal B is just the last signal that can be obtained using thermal analysis on these alloys. The residual liquid produces too small an amount of solid phase (or solidification enthalpy), spread over this final temperature range, to be detected even in a dedicated DSC or DTA experiment.

It is stressed that all the experimental data can be successfully interpreted by properly performed thermodynamic calculations, which supports the reliability of the present thermodynamic description.

6. Conclusions

In the present study, we firstly demonstrate the reliability of the thermodynamic description for the Mg–Al–Mn–

Zn system by comparison with the experimental data. The proper interpretation of the experimental results obtained by thermal analysis was then performed on the basis of thermodynamic calculations, indicating a widespread misinterpretation communicated in the previous literature. The following important points are clarified:

(i) The solidification process of Mg alloys such as AZ91 and AZ62 proceeds under non-equilibrium conditions even with a cooling rate as low as 1 K/min.
(ii) The high-temperature signal observed in thermal analysis does not represent the actual liquidus temperature. This signal is related to the phase boundary, $L + Al_8Mn_5/L + Al_8Mn_5 + (Mg)$.
(iii) The low-temperature signal in thermal analysis is not associated with the end of the solidification process. This signal corresponds to the temperature at which the precipitation of γ-$Mg_{17}Al_{12}$ phase starts under Scheil conditions.
(iv) The concept of NEST is used to demonstrate that the incipient melting temperature of as-cast Mg alloys is virtually identical to the solidification temperature under Scheil conditions. The present thermodynamic calculations can describe and predict the incipient melting and solidification temperatures of as-cast Mg alloys with quite a high accuracy. In the low-alloyed range the solidification proceeds closer to equilibrium conditions and the predictions show a larger uncertainty.

Finally, it is stressed that the well-established thermodynamic description enables the proper interpretation of experimental results obtained under equilibrium and non-equilibrium conditions. The current thermodynamic description is considered to be sufficiently scrutinized to apply computational thermochemistry as a tool to provide significant information for the design and development of Mg alloys in the AZ and AM series. Work is in progress to extend this to higher order Mg alloys.

Acknowledgements

The authors are grateful to Prof. R. Ferro at the University of Genova for performing the comparative DSC measurements (DSC2). This study was supported by the German Research Foundation (DFG) in the Priority Programme "DFG-SPP 1168: InnoMagTec" under Grant No. Schm 588/27.

References

[1] Kaufman L, Bernstein H. Computer calculation of phase diagrams with special reference to refractory materials. New York (NY): Academic Press; 1970.
[2] Chang YA, Chen SL, Zhang F, Yan X, Xie F, Schmid-Fetzer R, et al. Progr Mater Sci 2004;49:313.
[3] Ohno M, Schmid-Fetzer R. Z Metallkd 2005;96:857.
[4] Ohno M, Mirkovic D, Schmid-Fetzer R. Mater Sci Eng A 2006;421:328.
[5] Ohno M, Schmid-Fetzer R. Int J Mater Res (Z Metallkd) [in press].
[6] Gjestland HT. Competence Centre Magnesium, Hydro Aluminium Research Centre Porsgrunn. Norway. Private communication; 2005.
[7] Thorvaldsen A, Aliravci CA. Adv Prod Fabr Light Met Met Matrix Comp. In: Proceedings of the international symposium; 1992. p. 277.
[8] Busk RS, Marande RF. Trans Am Inst Min Metall Pet Eng 1946;166:346.
[9] Caceres CH, Davidson CJ, Griffiths JR, Newton CL. Mater Sci Eng A 2002;326:344.
[10] Cerri E, Barbagallo S. Mater Lett 2002;56:716.
[11] Lindemann A, Schmidt J, Todte M, Zeuner T. Thermochim Acta 2002;383:269.
[12] Wang Y, Sun B, Wang Q, Zhu Y, Ding W. Mater Lett 2002;53:35.
[13] Mirkovic D, Schmid-Fetzer R. Z Metallkd 2006;97:119.
[14] Liang P, Tarfa T, Robinson JA, Wagner S, Ochin P, Harmelin MG, et al. Thermochim Acta 1998;314:87.
[15] Miettinen J. Calphad 2001;25:43.
[16] Chen SL, Daniel S, Zhang F, Chang YA, Oates WA, Schmid-Fetzer R. J Phase Equilibria 2001;22:373.